Available online at www.sciencedirect.com

ScienceDirect

Journal of Electrical Systems and Information Technology 3 (2016) 485–512

www.elsevier.com/locate/jesit

Bacteria-foraging based-control of high-performance railway level-crossing safety drives fed from photovoltaic array

Essamudin A. Ebrahim

Power-Electronics and Energy-Conversion Department, Electronics Research Institute, El-tahrir Street, National Research Center Buildings, 12662, Dokki, Giza, Egypt

Received 30 August 2015; received in revised form 28 October 2015; accepted 2 November 2015
Available online 9 August 2016

Abstract

In the past ten years, railway level-crossing accidents have noticeably escalated in an indisputably preposterous manner, this devastating snag opened the floodgates for the frustrating death of a numerous number of the third world's citizens, especially in Egypt. To tackle with this problem, a fully intelligent control system is required, which must be automated without human intervention. So, in this research, a new proposed level-crossing tracking system is designed and introduced. The system comprises a high-performance induction motor (IM) fed from photovoltaic (PV) array, the boom barrier (gate) with its mechanism – as a load – buck–boost converter, inverter, and two smart PI-controllers. The first one is designed to regulate the duty cycle of the converter to its optimum value required to balance between maximum power point tracking (MPPT) and keeping dc-link voltage of the inverter at a minimum level needed to maintain the motor internal torque at rated value. The second PI-controller is designed for speed control of indirect field-oriented vector-control (IFO-VC) IM. The proposed design problems of MPPT, dc-link voltage and speed controllers are solved as optimization problems by bacteria-foraging optimization (BFO) algorithm to search for the optimal PI-parameters. The simulation test results are acquired when using the battery-less PV-array with and without the proposed controllers. Also, results are obtained when applying several prescribed speed trajectories to test the robustness against PV-irradiance fluctuations and motor-dynamic disturbances. From these results, the proposed intelligent controllers are robust compared to classical Ziegler–Nichols (ZN) PI-controllers and also when the motor is directly fed from PV generator without converter.

Keywords: High performance drives (HPDs); Induction motors (IMs); Level crossing; Bacteria foraging optimization (BFO); Indirect field-orientation (IFO); Photo voltaic (PV)

1. Introduction

In Egypt, there are more than 1200 railway level crossings with boom barriers. Most of these barriers are still operated manually by a gate keeper after receiving the information about the train's arrival.

E-mail addresses: essamudin@yahoo.com, essamudin@eri.sci.eg
Peer review under the responsibility of Electronics Research Institute (ERI).

Production and hosting by Elsevier

http://dx.doi.org/10.1016/j.jesit.2015.11.014

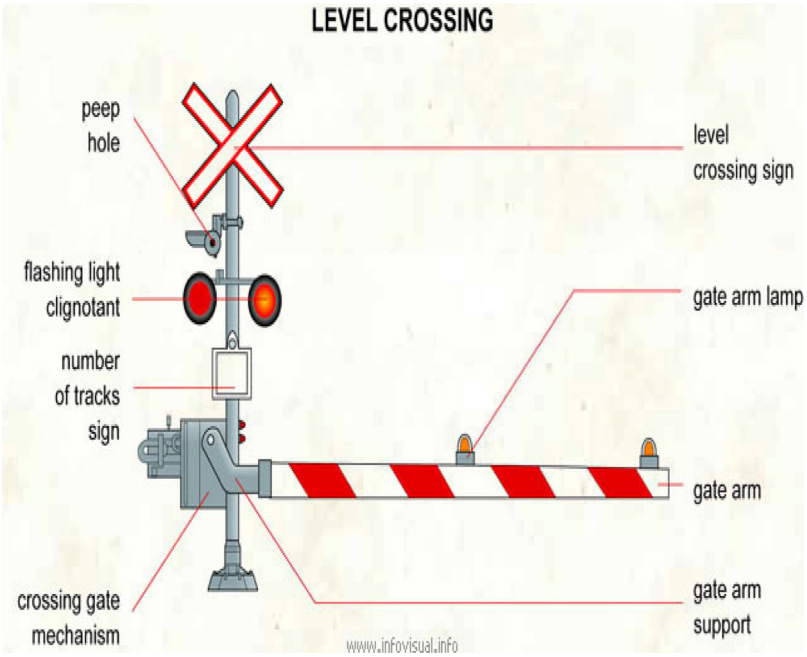

Fig. 1. The railway level-crossing system.

Due to human mistakes such as negligence of train drivers and gate keepers, many accidents occurred and gradually increased (Pu et al., 2014).

To overcome this problem, a fully intelligent control system (as shown in Fig. 1) is required, must be automated and not depend on human factors. The system requires vision sensors, host processor and electric machine drive for moving gate that is fed from a power supply or energy source.

Photovoltaic (PV) generation is gaining attention as a renewable clean source due to its advantages such as the absence of fuel cost and moving parts, little maintenance, no noise, wear and tear etc.

The output of the PV array is variable and there is a unique operating point at which its output power is maximized.

Tracking the maximum power point (MPP) of a PV array is usually an essential part of a PV system. As such many MPP tracking (MPPT) methods have been developed and implemented (Esram and Chapman, 2007).

Some classical techniques such as hill climbing, perturb and observe, incremental conductance, fractional open-circuit voltage (Masoum et al., 2002), current sweep, ripple correlation control (RCC), load current or load voltage maximization, and DC-link capacitor droop control, are proposed.

On the other hand, some advanced techniques such as Artificial Neural Network (ANN) and Fuzzy Logic Control (FLC) are used in MPPT (Kassem, 2011).

But, the level-crossing tracking system occasionally operates at a constant power for a few minutes only when the trains pass.

However, any proposed technique used with ac-motor drive fed from off-grid PV-array should balance between MPPT and dc-voltage stabilization of the link between converter/inverter set. By other words, the dc-link voltage must be regulated to maintain its value equal to a minimum level that delivers the required torque to the load (boom barrier) without oscillations or ripples.

In addition, IM is a non-linear plant that all parameters are time-variant and classical controllers are not robust to satisfy the high-performance in motor-tracking control.

Recently, the advent of evolutionary computation (EC) such as genetic algorithm (GA) (Oshaba et al., 2015), Particle Swarm Optimization (PSO) (Essamudin, 2015), germ of intelligent (as Ant Colony Optimization ACO (Abdul-ghaffar et al., 2014), Artificial Bee Colony (ABC) (Essamudin, 2016a,b), and Bacteria Foraging (BF) (Essamudin, 2015; Abdul-ghaffar et al., 2013; El-Saady et al., 2015) techniques) have inspired as new techniques for optimal design problems.

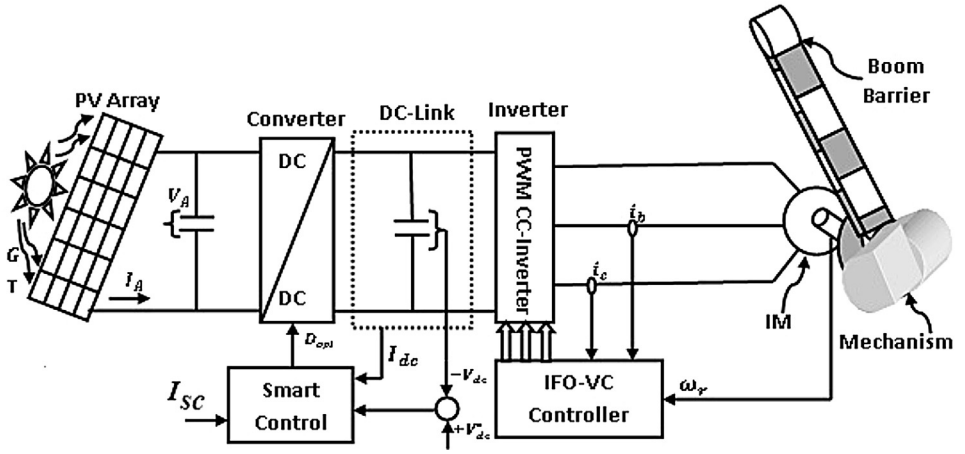

Fig. 2. The PV railway level-crossing tracking system.

In Egypt, the weather is flabbergasting and the sun is bright all over the course of the year but most PV motor-drive applications are pumping, watering and irrigation purposes.

Another different suggested PV-application is railway level-crossing. So this research proposes a new level-crossing IM-tracking system fed directly from off-grid PV array all the day through converter/inverter set. At night and cloudy days, a system is fed directly from storage elements that are charged when the tracking system is switched off through the same proposed converter. The research will focus only on the system when directly fed from PV without storage elements and charging process.

This paper introduces a new approach for designing two PI controllers based-on BF optimization algorithm to track both the PV power with dc-link voltage regulation and the motor speed of an indirect field-oriented vector-control (IFO-VC) three-phase high-performance induction motor. Also, a MPPT-algorithm that depends on the dc-link and PV short-circuit currents is proposed. A complete design for the boom barrier of the level crossing and its mechanism – as a motor load – is introduced.

Simulation results for several prescribed speed trajectories (including forward and reverse driving that mimic the movement of boom barrier, i.e., up and down) with PV irradiance fluctuations are proposed, simulated and evaluated to test the robustness of the proposed system. A comparison with a conventional Ziegler and Nichols (ZN) PI-controller is carried out to ensure the robustness and effectiveness of the proposed algorithm. Also, the obtained results insure the validity of the proposed technique with the most of high performance applications.

2. The proposed drive system

The proposed PV railway level-crossing tacking system is shown in Fig. 2. It consists of the renewable energy source that is represented by PV array, dc to dc buck–boost converter with its optimized controller, dc-link high-capacitance storage capacitor, PWM current-controlled (PWM-CC) inverter fed field-oriented vector control IM drive with its controller and the boom barrier with its mechanism as a load.

2.1. PV-array model

PV module is the fundamental power conversion unit of a PV generator system. The output characteristics of PV modules depend on the solar insolation, the cell temperature and the output voltage of the PV module. Moreover, mathematical modeling of PV module is continuously updated to enable researcher to enable researchers to have a better understanding of its working.

In an array, PV modules are connected in series and in parallel. It is important to consider the effects of those connections on the performance of the array. The output current I_A and output voltage V_A of a PV array with N_S cells in series and N_P strings in parallel can be determined from the following equation (Acakpovi and Hagan, 2013):

The total cell current can be computed as:

$$I = I_{\text{irr}} - I_o\left[e^{\left(\frac{q(V+IR_s)}{nkT}\right)} - 1\right] - \frac{V + IR_s}{R_p} \tag{1}$$

The total module current can also computed as:

$$I_M = I_{\text{irr}} - I_o\left[e^{\left(\frac{q(V_M+I_M N_s R_s)}{N_s nkT}\right)} - 1\right] - \frac{V_M + I_M N_s R_s}{N_s R_p} \tag{2}$$

Dependently, the total current of PV array is:

$$I_A = N_p I_{\text{irr}} - I_o\left[e^{\left(\frac{q\left(V_A + I_A \frac{N_s}{N_p} R_s\right)}{N_s nkT}\right)} - 1\right] - \frac{V_A + I_A\left(\frac{N_s}{N_p}\right) R_s}{\frac{N_s}{N_p} R_p} \tag{3}$$

$$V_A = \frac{N_s}{\Lambda} \ln\left[\frac{GN_P I_A - I_{\text{irr}}}{N_p I_o} + 1\right] - \frac{N_s}{N_p} R_s I_{pv} \tag{4}$$

and,

$$\Lambda = \frac{q}{\varepsilon KT} \tag{5}$$

Also, the total output of the PV array can be determined as:

$$P_A = V_A \times I_A \tag{6}$$

where,

P_A: Average module output power (W)
I, I_M, I_A: Cell, module, array currents (A)
I_{irr}: Irradiance or photo current (A)
I_o: The diode saturation current (A)
V, V_M, V_A: The cell, module and array voltages (V)
$q = 1.6 \times 10^{-19}$ C: The electron charge (C)
K = Boltzmann constant = $1.3806503 \times 10^{-23}$ J/K
R_s, R_p: Series and parallel resistance (Ω)
$N_s N_p$: Number of series and parallel cells
T = 298.15: The temperature of the cell (°K)
$\varepsilon = 1.1$: The completion factor
Λ: The solar cell constant
G: The solar insulation in per unit

For the proposed array, the number of PV-series cells are $N_s = 5$ and parallel cells are $N_p = 20$. The total number of PV-cells for the array (series and parallel are = $5 \times 20 = 100$ cells).

2.2. DC/DC buck–boost converter

The three basic switching DC/DC converter topologies in common use are the buck, boost, and buck–boost. Many converters have been used and tested; buck converter is a step down converter, while boost converter is a step up converter. The buck–boost is a popular non-isolated, inverting power stage topology, sometimes called a step-up/down power stage. So, in this work, the buck–boost converter is proposed. Fig. 3 shows a simplified schematic of the buck–boost power stage with a drive circuit block included. Where, S is an electronic switch as MOSFET or IGBT, D is a reverse diode, L is an inductor, C is a capacitor, R_L, R_C are the internal resistances for inductor and capacitor, and V_A, V_{dc} are the PV array voltage and the dc link output voltages. The output voltage and current for the converter can be determined from the following (Rogers, 2002):

$$V_{\text{dc}} = \frac{-D}{1 - D} \times V_A \tag{7}$$

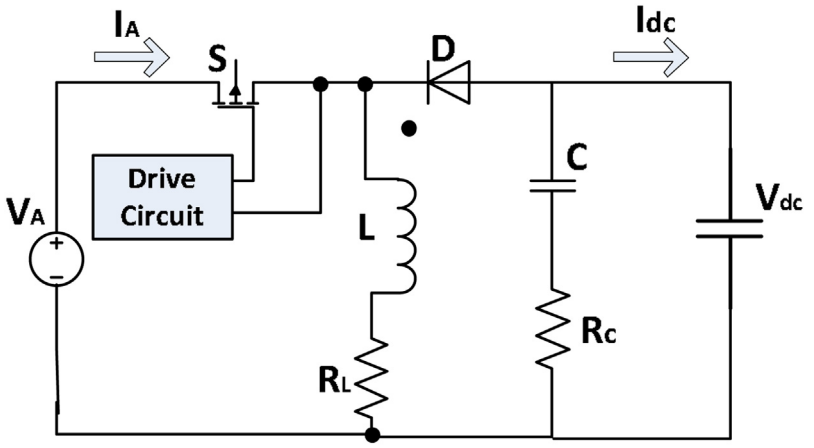

Fig. 3. Buck–boost power converter.

$$I_{\mathrm{dc}} = \frac{D-1}{D} \times I_A \tag{8}$$

where D is the duty cycle of the pulse width modulation (PWM) and I_{dc} is the dc link current.

2.2.1. Location of maximum power points (MPP)

At a maximum power point (MPP) (Masoum et al., 2002):

$$\frac{\mathrm{d}P_A}{\mathrm{d}V_A} = \frac{\mathrm{d}(V_A I_A)}{\mathrm{d}V_A} = 0 \tag{9}$$

Therefore,

$$I_A + V_A \frac{\mathrm{d}I_A}{\mathrm{d}V_A} = 0 \tag{10}$$

By substituting from Eqs. (3) and (4) in Eq. (10) and linearizing the relationship which approximately is:

$$I_A = I_{\mathrm{MPP}} \cong 0.94 I_{\mathrm{sc}} \tag{11}$$

where I_{MPP} is the array output current at a MPP and I_{sc} is a short circuit current for the PV array.

By substituting in Eq. (8) from Eq. (11):

$$I_{\mathrm{dc(MPP)}} \cong 0.94 I_{\mathrm{sc}} \frac{(D_{\mathrm{opt}} - 1)}{D_{\mathrm{opt}}} \tag{12}$$

Finally, the dc-link current is function of both short-circuit current of the array and duty cycle of the converter. The relation between dc-link current and optimum duty cycle can be plotted to give MPP (as shown in Section 5).

So, both the MPPT achievement and dc-link voltage regulation can be balanced to verify optimum operation by adjusting the duty cycle of the converter.

2.2.2. The proposed optimized controller

In order to optimize the operating point for the dc converter with PV array, a proposed intelligent PI-controller is used. The operating range of the controller is optimized by tuning the PI controller parameters; K_p and K_i at different operating points. A bacteria-foraging optimization (BFO) algorithm is used to set the optimal values of the controller parameters based on the optimized algorithm of objective function.

The tuning process aims to minimize rise time, settling time, ripple and steady-state error of the output voltage for the dc converter. Optimal values for the PI-controller parameters are computed and then self-adapted with fine tuning to achieve MPPT. Fig. 4 represents this proposed controller.

BFO strategy, algorithm, and activation or objective function will be explained later.

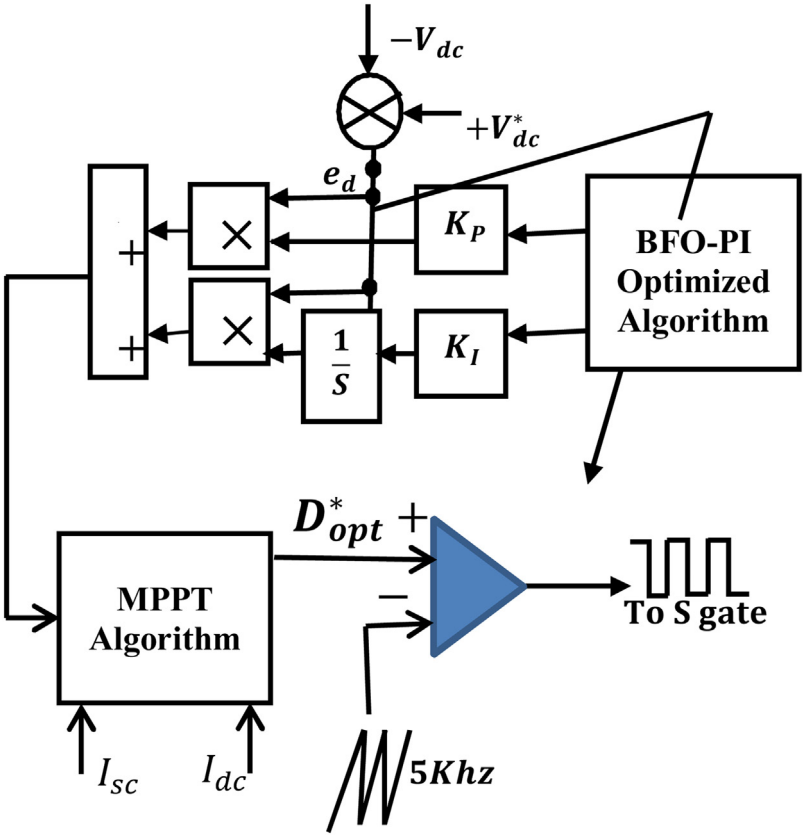

Fig. 4. The proposed PV-PI-BFO controller.

The outputs of the BFO-algorithm are both the optimized proportional and integral gains of the PI-controller. Because of the controllability of dc-link voltage, it is considered as a constant. So, dc-link current is changed according to the motor current. Dependently, the optimized duty cycle is released to balance between MPPT and dc-link voltage stabilization. The PI-controller model is given as:

$$\left.\begin{aligned} u(t) &= K_p e_d(t) + K_i \int_0^\infty e_d(t) \\ U(S) &= K_p E(s) + \left(\frac{K_i}{S}\right) E(s) \end{aligned}\right\} \tag{13}$$

where $e_d = V^*_{\mathrm{dc}} - V_{\mathrm{dc}}$.

V^*_{dc} and V_{dc} are the reference and actual dc-link voltage of converter/inverter set.

This reference duty cycle is compared with triangular high frequency signal. Finally, the output is a square wave with variable duty cycle D. So, D_{opt} is adapted according to the controller decision to change the operating point to its optimal value.

2.3. Design of boom barrier

The barrier is made of iron with density equal ($\rho = 7870\,\mathrm{kg/m^3}$) and its length is selected equal to ($\ell_b = 5\,\mathrm{m}$) and consists of two parallel bars with a distance between them equal to ($d = 20\,\mathrm{cm}$). Both of them are joined with each other by welding across small bars. All bars are equidistance and equal ($e_b = 1\,\mathrm{m}$) with total numbers equal ($n_b = 4$).

The cross-section of the bar equal to ($a = \pi r^2$), where, r is the radius of the bar-cross-section and equal ($r = 0.004\,\mathrm{m}$).

Then the total volume and weight of the barrier can be computed as:

$$\text{Volume } = v = a\ell t \; (\ell t = \; 10.8\,\text{m})$$

$$\text{Weight-}w\text{-mg } = \rho \times v = \rho g a \ell t$$

where $g = 9.8\,\text{m/s}^2$.

Finally, the total weight of the barrier equals ($w_b = 41.8\,\text{N}$). If it turns from horizontal position to vertical, this means that it turns by 90°, it requires a certain rotational torque T_L to move it up and down.

Where, $T_L = w_b \times x$, and x is the average distance that it moves. Then, the total required-mechanical torque is computed and approximately equal to (80 Nm). So, the induction motor of (5.4 HP) rated output power is suitable and sufficient to drive the load with a gear box of turns ratio (n) 2:1.

2.4. IM mathematical dynamic model

The three-phase induction motor is still very attractive for a wide range of applications due to its advantages such as robustness, simple construction, no maintenance, high power to weight ratio and low cost (Essamudin, 2001; Essamudin and Hammad, 2003). In this study, the dq-axis model of a three-phase IM with the reference axes rotating at synchronous speed is used. The following equations are obtained in the synchronous reference frame (Essamudin and Hammad, 2003):

$$v_{ds}^{e} = R_s i_{ds}^{e} + p\lambda_{ds}^{e} - \omega_s \lambda_{qs}^{e} \tag{14}$$

$$v_{qs}^{e} = R_s i_{qs}^{e} + p\lambda_{qs}^{e} + \omega_s \lambda_{ds}^{e} \tag{15}$$

$$v_{dr}^{e\prime} = R_r' i_{dr}^{e\prime} + p\lambda_{dr}^{e\prime} - (\omega_s - \omega_r)\lambda_{qr}^{e\prime} \tag{16}$$

$$v_{qr}^{e\prime} = R_r' i_{qr}^{e\prime} + p\lambda_{qr}^{e\prime} + (\omega_s - \omega_r)\lambda_{dr}^{e\prime} \tag{17}$$

$$\lambda_{ds}^{e} = L_s i_{ds}^{e} + L_m i_{dr}^{e\prime} \tag{18}$$

$$\lambda_{ds}^{e} = L_s i_{\text{qs}}^{e} + L_m i_{qr}^{e\prime} \tag{19}$$

$$\lambda_{dr}^{e\prime} = L_r' i_{dr}^{e\prime} + L_m i_{ds}^{e} \tag{20}$$

$$\lambda_{qr}^{e\prime} = L_r' i_{qr}^{e\prime} + L_m i_{qs}^{e} \tag{21}$$

$$T_e = \frac{3}{4}\frac{PL_m}{L_r'}\left(i_{qs}^{e}\lambda_{dr}^{e\prime} - i_{ds}^{e}\lambda_{qr}^{e\prime}\right) \tag{22}$$

$$T_e = J\left(\frac{\mathrm{d}\omega_m}{\mathrm{d}t}\right) + B_f\omega_m + T_L \tag{23}$$

where v_{sdq}^{e}, i_{sdq}^{e}, λ_{sdq}^{e}, R_s, L_s are the stator voltage, current, flux, resistance, and inductance vectors in dq-synchronous reference frame respectively.

$v_{rdq}^{e\prime}$, $i_{rdq}^{e\prime}$, $\lambda_{rdq}^{e\prime}$, R_r', L_r' are the rotor voltage, current, flux, resistance, and inductance vectors referred to the stator in dq-synchronous reference frame respectively.

Also, p, ω_r, ω_s, ω_m, T_e, T_L, P, B_f, J and L_m are the differential operator (d/dt), rotor electrical angular speed, synchronous electrical angular speed, rotor mechanical speed, electrical internal torque, mechanical load torque, no. of poles, viscous friction coefficient of the motor, the rotor mass moment of inertia, the stator resistance, the rotor resistance, the stator inductance, and the self or mutual inductance between the stator and rotor respectively.

2.4.1. Indirect rotor-flux field-oriented vector-controlled scheme

The field orientation concept implies that the current components supplied to the machine should be oriented in phase (flux component) and in quadrature (torque component) to the rotor flux vector. This is accomplished by choosing ω_s to be the instantaneous speed of rotor flux and locking the phase of the reference system such that the rotor flux

is entirely in the d-axis (flux axis), resulting in the mathematical constraints (Essamudin, 2016b; Boldea and Nasar, 2000):

$$\lambda_{qr}^{e\prime} = 0 \tag{24}$$

So, by substituting in Eq. (22) yields:

$$T_e = \frac{3}{4}\frac{PL_m}{L_r'}\left(i_{qs}^{e}\lambda_{dr}^{e'}\right) = K_T i_{qs}^{e}\lambda_{dr}^{e'} \tag{25}$$

where $K_T = (3/4)(PL_m/L_r')$.

For rotor short circuit and constant direct rotor flux, $v_{dr}' = v_{qr}' = 0$, and $\lambda_{dr}^{e\prime}$ = constant, by substituting in Eqs. (21) and (17)

$$\omega_{sl} = s\omega_s = (\omega_s - \omega_r) = \text{slip speed}$$

$$\omega_{sl} = \frac{R_r' L_m}{L_r'}\frac{i_{qs}^{e}}{\lambda_{dr}^{e\prime}} = \frac{1}{\tau_r}\frac{i_{qs}^{e}}{i_{ds}^{e}}(\text{at steady state}) \tag{26}$$

where the transfer function $G(p)$ can be obtained:

$$\mathrm{G}(p) = \frac{L_M}{1 + p\tau_r} \quad \text{and} \quad \left(\tau_r = \frac{L_r'}{R_r'}\right)$$

For, indirect field-oriented rotor-flux vector control, the rotor flux angle θ_{rf} in the stator stationary reference frame ($\alpha\beta$ − referenceframe) can be computed as:

$$\theta_{rf} = \int_0^t (\omega_{sl})\,\mathrm{d}t + \theta_r \tag{27}$$

Then, the dq-$\alpha\beta$ transformation is expressed as:

$$\begin{bmatrix} i_{\alpha s}^{s*} \\ i_{\beta s}^{s*} \end{bmatrix} = \begin{bmatrix} \cos(Q_{rf}) & -\sin(Q_{rf}) \\ \sin(Q_{rf}) & \cos(Q_{rf}) \end{bmatrix} \begin{bmatrix} i_{\mathrm{ds}}^{\mathrm{e}*} \\ i_{\mathrm{qs}}^{\mathrm{e}*} \end{bmatrix} \tag{28}$$

Finally, use the following equation to compute three-phase reference currents i_{as}^*, i_{bs}^*, i_{cs}^*:

$$\begin{bmatrix} i_{as}^{*} \\ i_{bs}^{*} \\ i_{cs}^{*} \end{bmatrix} = \begin{bmatrix} 1 & 0 \\ -\frac{1}{2} & \frac{\sqrt{3}}{2} \\ -\frac{1}{2} & -\frac{\sqrt{3}}{2} \end{bmatrix} \begin{bmatrix} i_{\alpha s}^{s*} \\ i_{\beta s}^{s*} \end{bmatrix} \tag{29}$$

Finally, the block diagram of indirect filed-oriented vector controller (IFO) is shown in Fig. 5.

2.4.2. *Ramp-comparison current-controlled PWM inverter*

The proposed system uses a ramp comparison current controlled-PWM inverter as shown in Fig. 6 for only one phase (phase a) (Boldea and Nasar, 2000). The controller produces a sine-triangle PWM with the current error as the modulation function. The inverter switches depend on the frequency of the triangular wave. Six pulses for the three-phases are required to trigger the inverter legs known as (A+, A−, B+, B−, C+, C−).

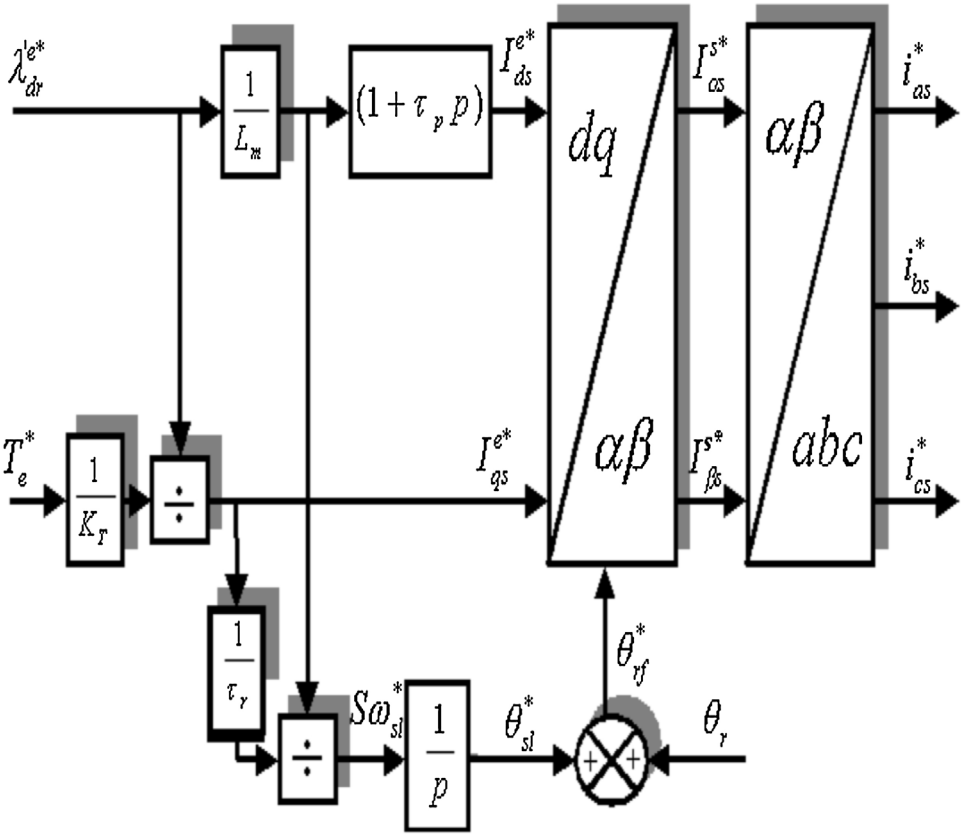

Fig. 5. Block diagram of IFO controller.

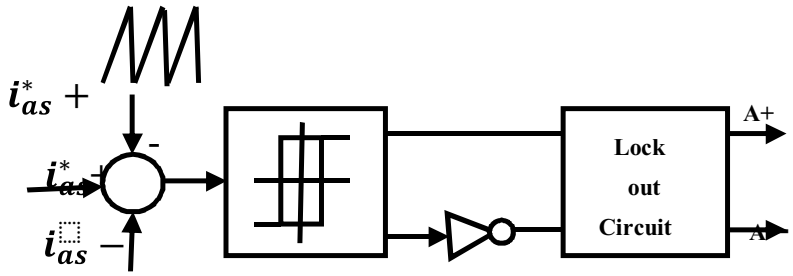

Fig. 6. Ramp comparison controller (phase *a* only).

2.5. Proposed PI-speed controller using BFO

The speed controller uses PI-BFO tuning as shown in Fig. 7. The output of the controller is:

$$T_e^*(t) = K_p e_r(t) + K_i \int_0^\infty e_r(t)\,\mathrm{d}t \tag{30}$$

where $e_r = \omega_r^* - \omega_r$.

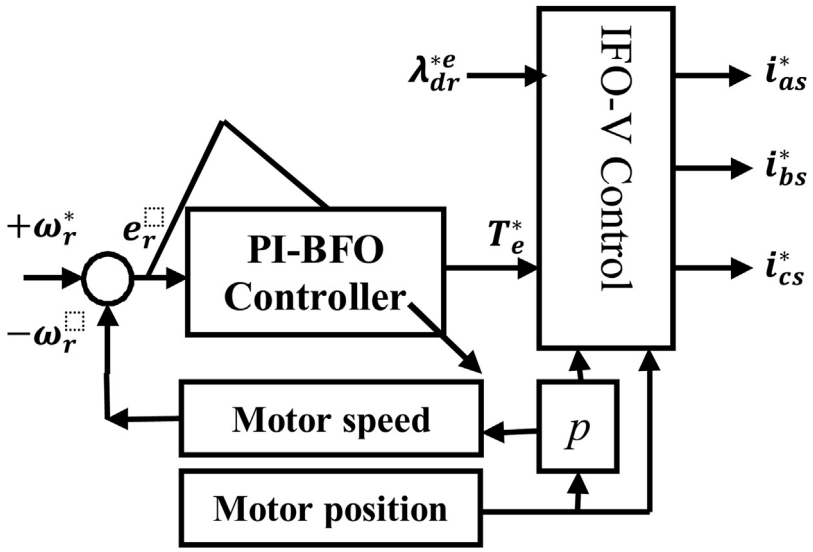

Fig. 7. The proposed BFO-PI speed controller.

The gains of the PI-controller are computed and optimized according to the objective function through BFO-algorithm that discussed in Section 4.

Then, the reference internal electrical torque is used in IFO-V control algorithm to compute the three-phase stator currents.

3. Bacteria foraging optimization (BFO)

3.1. A brief overview

The foraging strategy of *Escherichia coli* bacteria present in human intestine can be explained by four processes, namely chemotaxis, swarming, reproduction, and elimination–dispersal (Passino, 2002).

3.2. BFO-algorithm

3.2.1. Step 1—initialization

i Number of parameters (p) to be optimized.
ii Number of bacteria (S) in the population.
iii Swimming length N_S after which tumbling of bacteria will be undertaken in a chemotactic loop.
iv N_C the number of chemotactic steps ($N_C > N_S$).
v N_{re} the number of reproduction steps.
vi N_{ed} the number of elimination and dispersal events.
vii P_{ed} the probability of the elimination and dispersal bacteria.
viii The location of each bacterium $P(i, j, k)$ which is specified $P(i, j, k) = \{\theta^i (j, k, l)$ for $i = 1,2,\ldots, S\}$
ix The value of $C(i)$ which is assumed to be constant in our case for all the bacteria to simplify the design strategy.

3.2.2. Step 2—iterative algorithm for optimization

This section represents the bacterial population chemotaxis, swarming, reproduction, elimination and dispersal (initially, $j = k = l = 0$). For the algorithm updating θ^i automatically results in updating of 'P'.

1) Elimination-dispersal loop: $l=l+1$
2) Reproduction loop: $k=k+1$
3) Chemotaxis loop: $j=j+1$
a) For $i=1, 2, \ldots, S$, calculate cost function value for each bacterium i as follows.

- Compute value of cost function $J(i, j, k, l)$.

Let

$J_{sw}(i, j, k, l) = J(i, j, k, l) + J_{cc}(\theta^i(j, k, l), P(j, k, l))$

($J_{cc}(\theta^i)$ is used to model the cell-to-cell signalling).

- Let $J_{last} = J_{sw}(i, j, k, l)$ to save this value since we may find a better cost via a run.
- End of For loop.

b) For $i=1,2,\ldots S$ take the tumbling /swimming decision

- Tumble: Generate a random vector $\Delta(i) \in \mathcal{R}^p$ with each element (i) $m=1,2,..p$.
- Move: let

$$\theta^i(j+1,k,l) = \theta^i(j,k,l) + C(i)\frac{\Delta(i)}{\sqrt{\Delta^T(i)\Delta(i)}}$$

- Compute $J(i, j+1, k, l)$

- Swim:

i) Let m=0; (counter for swim length).
ii) While m< N_s (have not climbed down too long)

- Let m=m+1
- Compute $J_{sw}(i,j+1,k,l)$
- If $J_{sw}(i,j+1,k,l) < J_{last}$, let

$$J_{last} = J_{sw}(i,j+1,k,l) \text{ and then}$$
$$\theta^i(j+2,k,l) = \theta^i(j+1,k,l) + C(i)\frac{\Delta(i)}{\sqrt{\Delta^T(i)\Delta(i)}}$$

and use the equation $(\theta^i(j+1,k,l))$ to compute the new $J(i,j+1,k,l)$

- Else, let $m=N_s$. this the end of the while statement.
- Go to the next bacterium (i+1) if $i \neq S$ (i.e. go to b) to process the next bacterium .

4) If $j<N_c$, go to (3). In this case, continue chemotaxis since the live of the bacteria is not over.
5) Reproduction
   a) For the given k and l, and for $i=1,2,..S$, let $J^i_{health} = min\{J_{sw}(i,j,k,l)\}$ be the health of the bacterium i (a measure of how many nutrients it got over its life time and how successful it was at avoiding noxious substance). Sort bacteria in order of ascending cost J_{health} (higher cost means lower health).
   b) the S_r=S/2 bacteria with highest J_{health} value die and other S_r bacteria with the best value split (and the copies that are made are placed at the same location as their parent).
6) If $k < N_{re}$ go to 2, in this case we have not reached the number of specified reproduction steps, so we start the next generation in the chemotactic loop.
7) Elimination-dispersal: For $i=1,2,..S$, with probability P_{ed}, eliminates and disperses each bacteria (this keeps the number of bacteria in the population constant) to a random location on the optimization domain.

4. Formulation of objective function

The target of the controller is minimizing speed and dc-link voltage errors with high dynamic performance. To improve speed and voltage time responses, due to dynamic disturbances, the overshoot, settling time and rise time should be minimized. In this study, Integral of Squared Error (ISE) is used as a cost function to be minimized. ISE accounts mainly for error at the beginning of the response and to a lesser degree for the steady state duration (Abdul-ghaffar et al., 2013).

$$\text{ISE} = \int_0^\infty \left(e^2\right) \mathrm{d}t \tag{31}$$

where,

$e_r(t) = \omega_r^* - \omega_r$ or $e_d(t) == V_{dc}^* - V_{dc}$

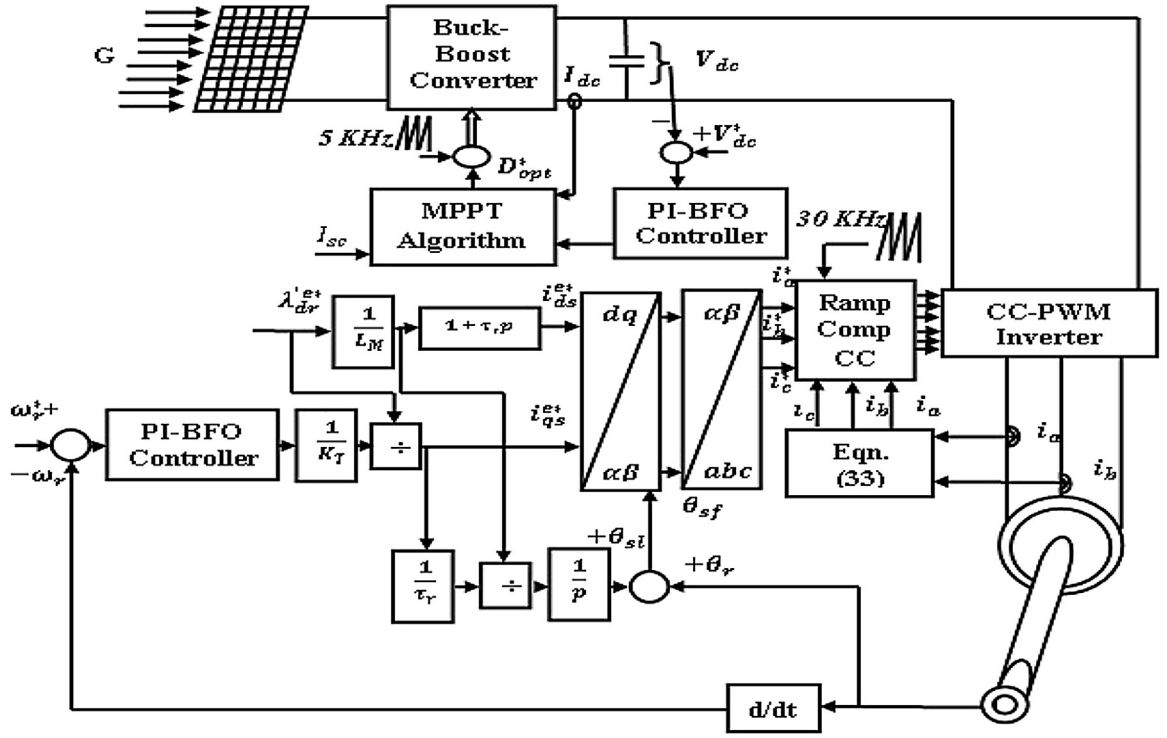

Fig. 8. The overall proposed PV tracking high performance IM drive with boom barrier.

ω_r^* = reference rotor speed rad/s
ω_a = actual rotor speed rad/s
V_{dc}^* = reference dc-link voltage V
V_{dc} = actual dc-link voltage V

This objective function is used—through bacteria foraging optimization algorithm in both dc-link voltage and speed control of the motor to achieve minimum error and optimize the PV and dynamic performance of the motor.

Therefore, the design problem can be formulated as the following optimization problem:

Minimize J subject to:

$$\mathrm{z}^{\min} \le \mathrm{z} \le \mathrm{z}^{\max} \tag{32}$$

where, z is a vector, which consists of the parameters of the PI-controller $\left(K_p, K_i\right)$.

$$K_{p1}^{\min} \le K_{p1} \le K_{p1}^{\max}, K_{p2}^{\min} \le K_{p2} \le K_{p2}^{\max}$$

$$K_{i1}^{\min} \le K_{i1} \le K_{i1}^{\max}, K_{i2}^{\min} \le K_{i2} \le K_{i2}^{\max}$$

5. Simulation results and discussion

The overall proposed system that is simulated and tested is shown in Fig. 8. The parameters and nameplate data are tabulated in Appendix A.

The motor rated current is approximately tracking drive used is 5.4 Hp induction motor with all equal 8.5 A and the rated line voltage is 400 V and the load torque is considered constant and equal to 30 Nm. The minimum dc-link voltage required to drive the inverter to feed the motor with beam barrier as a constant load is set to $400\sqrt{2}$ V = 565 V. Under these conditions, the PV module is selected with 96 cells and the no. of minimum series and parallel modules in the string are selected – for the worst case – as the minimum output power at the smallest irradiation of the module that

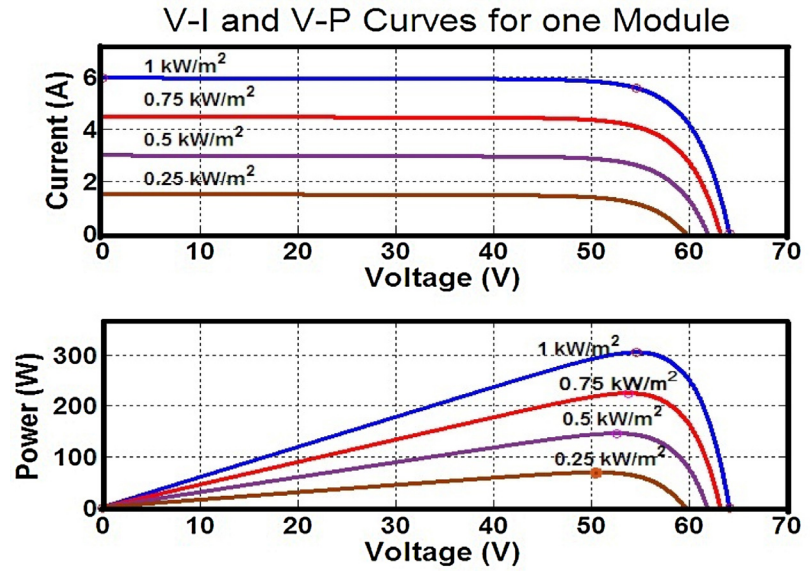

Fig. 9. Characteristic curves of one module.

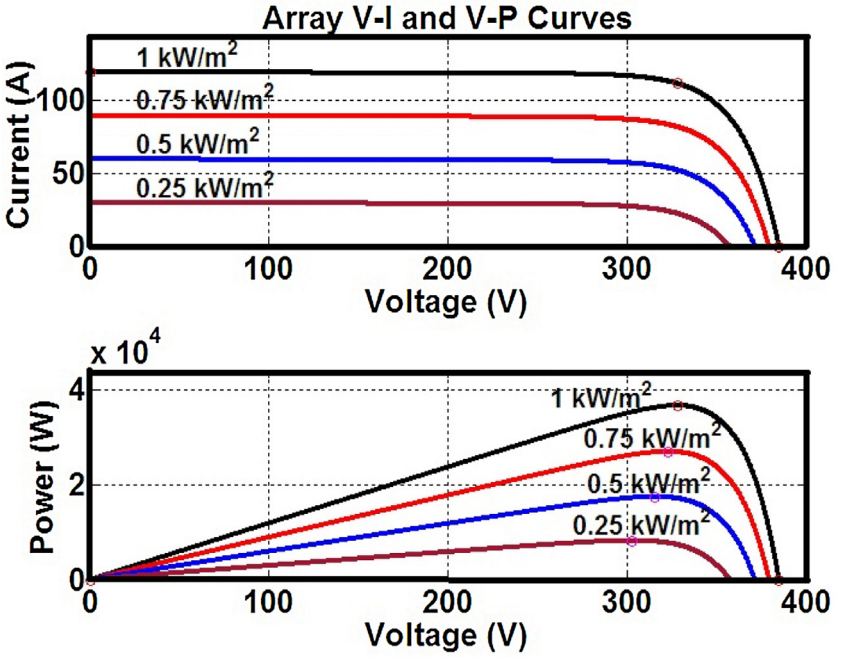

Fig. 10. Characteristic curves of the array.

equal 250 W/m^2. The V–P and V–I characteristics for both one used module and the array are shown in Figs. 9 and 10 respectively. The value of $N_s = 5$ and $N_p = 20$.

The limiting minimum and maximum values for both K_{p1} and K_{i1} are ranging from (10 to 60), (400 to 600) respectively and also for both K_{p2} and K_{i2} (5 to 15) and (10 to 30) respectively. The BFO algorithm parameters are organized in Appendix A. The proposed system is simulated using Matlab/Simulink Software package with the help of M-function in BFO-algorithm computation (Mathwork Corporation, 2012).

Table 1 includes a sample for self-adaptation and tuning for the proposed PI-BFO dc-link voltage controller.

The MPPT algorithm is summarized in Table 2.

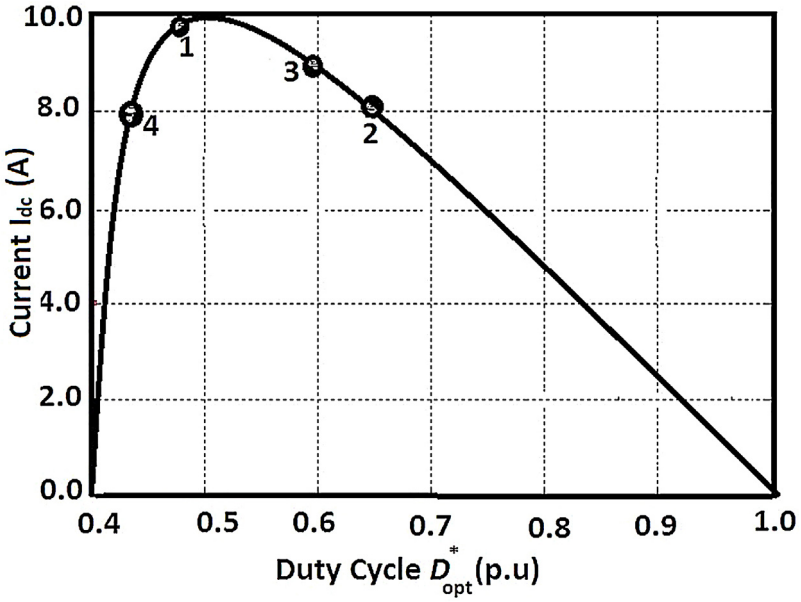

Fig. 11. D^*_{opt} versus I^*_{dc}.

Table 1
Optimal values of PI-controller parameters.

I_{dc} range	K_{p1}	K_{i1}
0.00–2.0	48.21	502.11
2.0–4.0	48.87	502.63
4.0–6.0	49.19	503.18
6.0–8.0	49.62	503.87
8.0–10.0	48.52	502.72

Table 2
Operating direction of D^*_{opt}.

Operating point in Fig. 11	Current states		Operating direction of D^*_{opt}
	I_{dc}	D^*_{opt}	
(1)	Positive	Increase	Hold on
(2)	Negative	Increase	Turn over
(3)	Positive	Decrease	Hold on
(4)	Negative	Decrease	Turn over

The algorithm scenario depends on 4 operating points on the I_{dc}–D^*_{opt} curve that show the direction of increasing or decreasing both the current and duty cycle.

Two current sensors are used with IM to feed the phases currents a and b. The third-phase current c can be computed from the equation:

$$i_c = -(i_a + i_b) \tag{33}$$

The effect of the temperature on the module is neglected and considered as a constant at 25 °C.

To study the effect of the PV insolation, it will be changed and varied as a ramp up and down or step in variation. Also, to study the robustness of the proposed controllers against dynamic variation and PV fluctuations, several speed trajectories are proposed. The motor input and output mechanical and electrical parameters are plotted for each case.

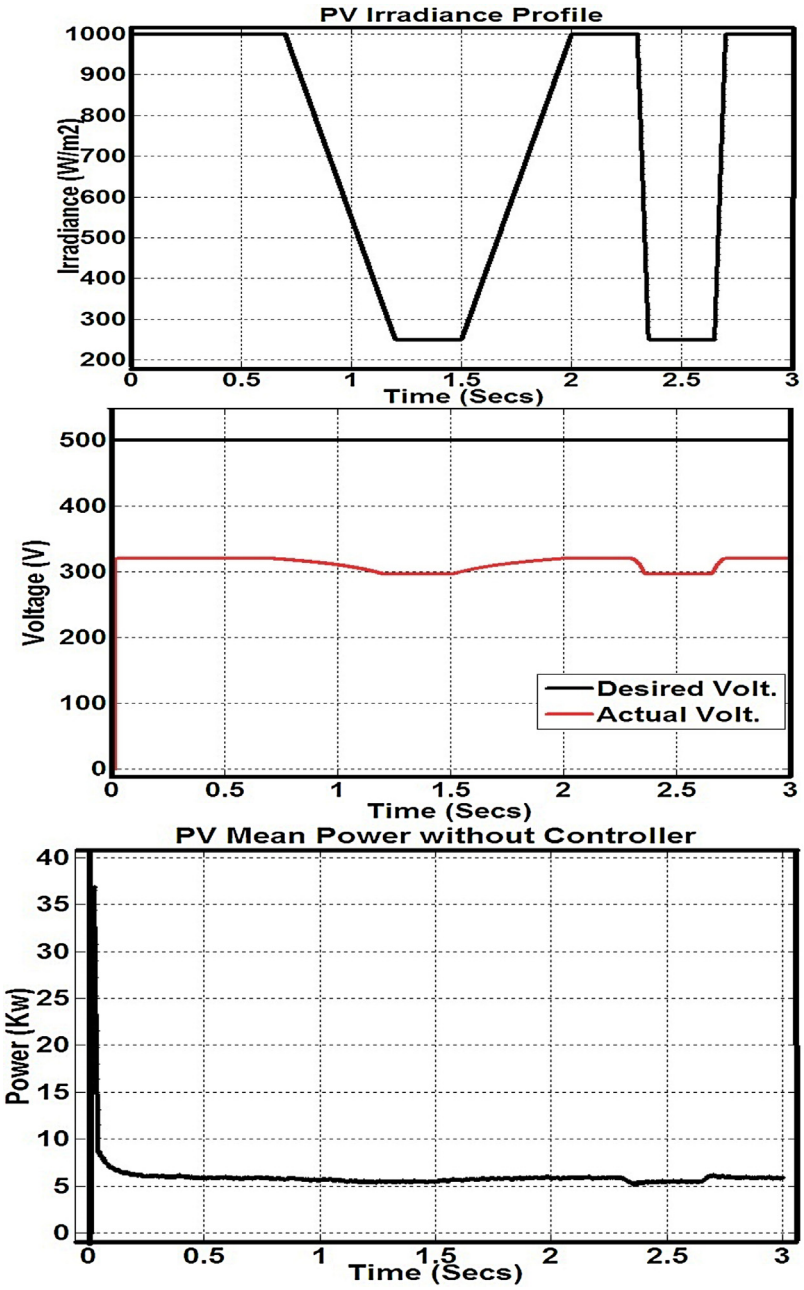

Fig. 12. PV insolation, voltage and power without converter.

5.1. Case 1: feeding directly from PV array without using converter

This case is simulated to study the effect of the proposed buck–boost converter on dc-link voltage regulation. Fig. 12 shows the PV inputs and outputs (i.e., irradiation or insolation, voltage and mean power). A required dc-link voltage is plotted against PV output and there is a great gap between both of them. This is an indication for the importance of the converter.

In this case, the motor reference speed is constant at 100 rad/s and both ref. and actual speed are shown in Fig. 1. Also, the motor phase currents, load and internal torque are shown in Fig. 13b and c.

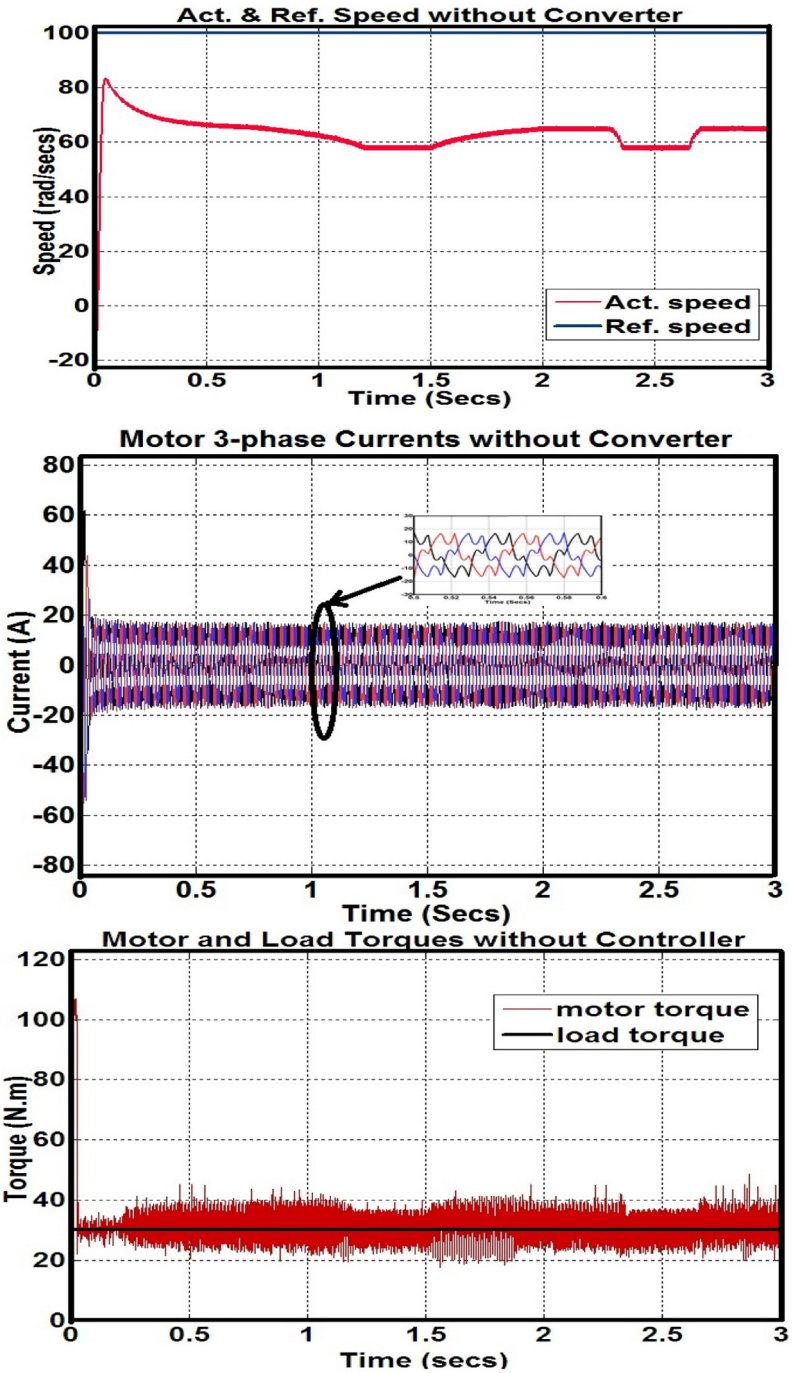

Fig. 13. Motor speed, current and torque without converter.

It can be noticed that the motor actual speed is very low and it could not reach the reference value due to low dc-link voltage of the inverter.

Also, the current waveforms are much distorted and the maximum values are greater than the rated values due to overloading to compensate the voltage drop in the dc link and the torque required. Also, there are so many ripples on torque waveform.

5.2. Case 2: using converter with dc-link voltage controller (PI-ZN controller)

In this case, the PV output is controlled by using the converter and the dc-link output voltage is controlled by using the classical Ziegler–Nicholas PI controller. This is called as PI-ZN controller.

The values of PI gains are equal ($K_p = 61.6$ and $K_i = 698.2$) for voltage controller and ($K_p = 11.5$ and $K_i = 26.3$) for speed controller.

Fig. 14 shows the PV input, outputs and optimum duty cycle profile with time. As shown, the output dc-link voltage has a maximum overshoot approximately 5% of steady-state value.

But finally it reached to steady state in approximately 0.3 s.

Fig. 15 illustrates the actual, reference speed, phase currents, load and motor torques. Also, it can be observe overshot of actual speed and the motor internal torque has many ripples.

The motor phase current is reduced when using the converter with the controller due to increasing in the terminal voltage of the inverter dc-link. Also, the current waveform is improved and becomes less distortion. The motor rated line voltage is 400 V, so the dc-link reference voltage must more or equal to the $\sqrt{2}$ of the line voltage (i.e., $V_{dc}^{*} = 400\sqrt{2} \cong 565$ V).

5.3. Case 3: response with PI-BFO controller

In this case, the proposed PI-BFO controller is tested with the PV system for the same conditions in the above two cases. Fig. 16 shows the same PV parameters (irradiance, voltage, mean power, and duty cycle). The dc-link voltage time response is improved and it can be noticed that the maximum overshot is minimized to the lower value (i.e., overshot becomes approximately 1%), then oscillated and finally it is damped to a steady state value. For the power, the mean power is minimized due to the proposed MPPT algorithm.

On the other hand, Fig. 17 represents the main motor variables. In this figure, it can be noticed that the motor actual and reference speed and the effect of the proposed controller on the response of motor speed. Also, the motor internal ripple torque is minimized to the lowest value. Beside this, the motor phase current waveform is improved and becomes sinusoidal without any distortion. Also, the value is minimized due to increase in the dc-link voltage of the inverter with the proposed controller.

To test the robustness of the proposed speed controller, several speed trajectories are proposed. Two speed trajectories are simulated: square-wave and saw-tooth. These proposed trajectories take into consideration, the movement of the boom barrier in the two-quadrant directions: one to open the gate and the other direction to close it (forward and reverse driving).

5.4. Case 4: robustness test with several speed trajectories

5.4.1. Square-wave speed trajectory

The reference speed of square wave has constant values (±100 rad/s) and the periodic time is 2S. The first half-wave value is a negative and then positive and repeated as shown in Fig. 19. Fig. 18 shows the PV irradiance and power. Also, the dc-link actual and reference voltages are shown. The duty cycle of the converter is varied according the insolation and trajectory as shown in Fig. 18.

On the other hand, the actual and reference speed trajectories are matched with each other and this illustrates the effect of the proposed controller (Fig. 19). Also, it can be noticed the motor-phase currents and internal torque in Fig. 19. There are only transition spikes through speed changing. The current waveform is a pure sinusoidal without distortion. The motor internal torque has approximately no ripples. However, this insures the robustness of the proposed controller in tracking.

5.4.2. Saw-tooth wave speed trajectory

In this section, the time response for the dc-link voltage with the proposed controller under saw-tooth wave speed trajectory is shown in Fig. 20. Also, this figure shows the PV irradiance profile, the mean power, optimum duty cycle, dc-link reference and actual voltages.

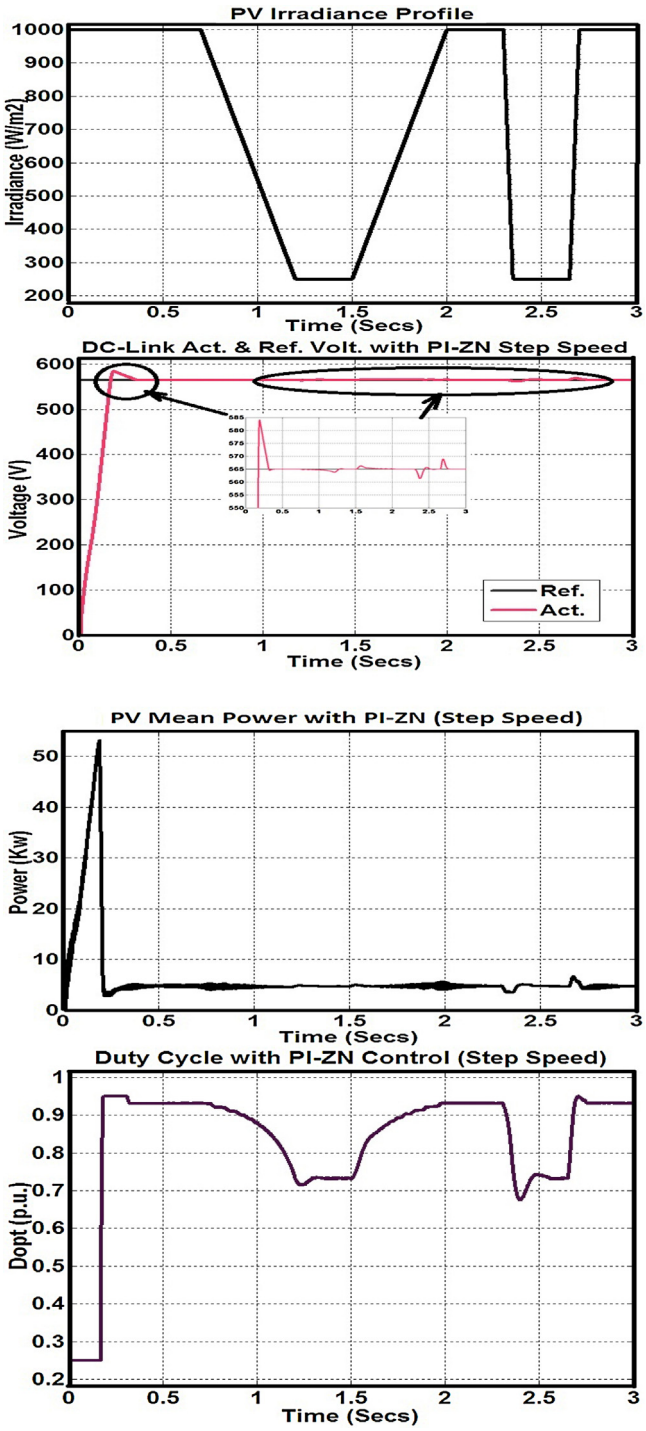

Fig. 14. PV irradiance, dc-link ref. and actual.

Fig. 21 includes actual and reference speed trajectories as a saw-tooth wave form. The motor tracks the prescribed trajectory with slight deviation through changing of the motor speed. From Figs. 20 and 21, both proposed PI-BFO controllers are robust against PV fluctuations and speed changing.

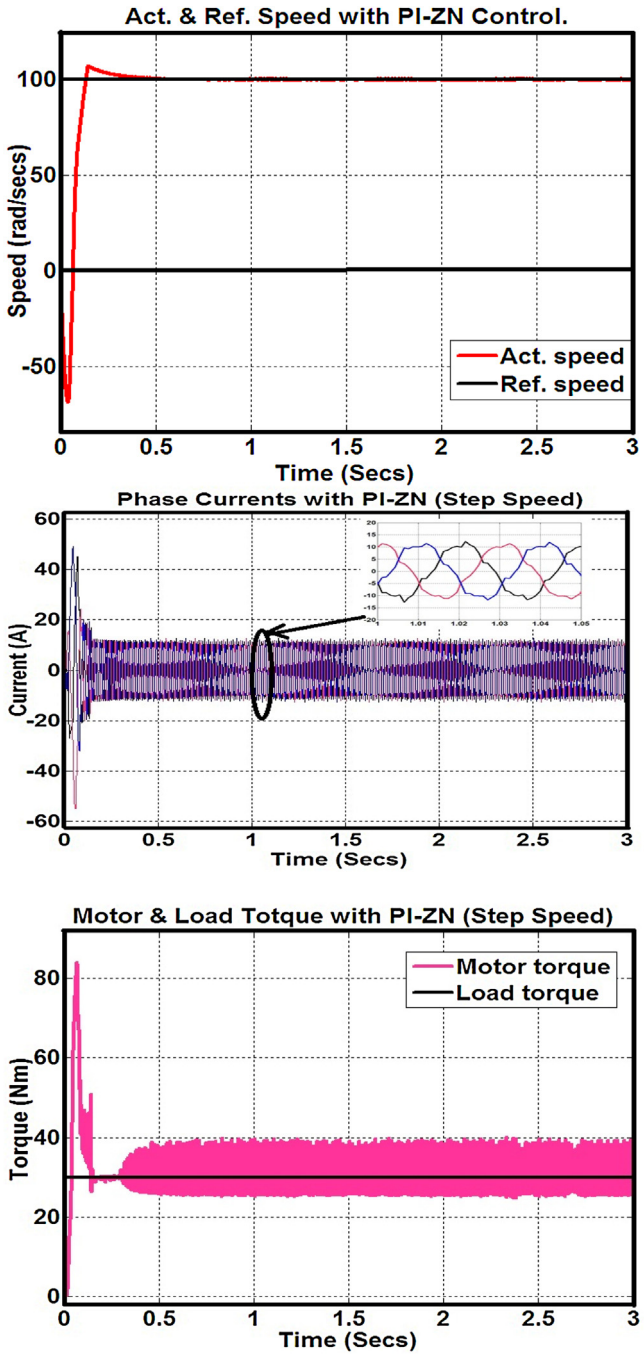

Fig. 15. The motor actual, reference speed, currents, motor and load torques with PI-ZN controller.

5.5. A comparison between PI-ZN and PI-BFO controllers

To explicate the effect of the proposed controllers on the dc-link voltage constancy and motor speed, this section will focus on the difference between the proposed PI-BFO and PI-ZN controllers.

Firstly, Fig. 22 presents the actual and reference dc-link voltage curves with both PI-BFO and PI-ZN controllers. Lucidly, there is a significant difference between both of them, especially, through starting period and the zone of low-insolation.

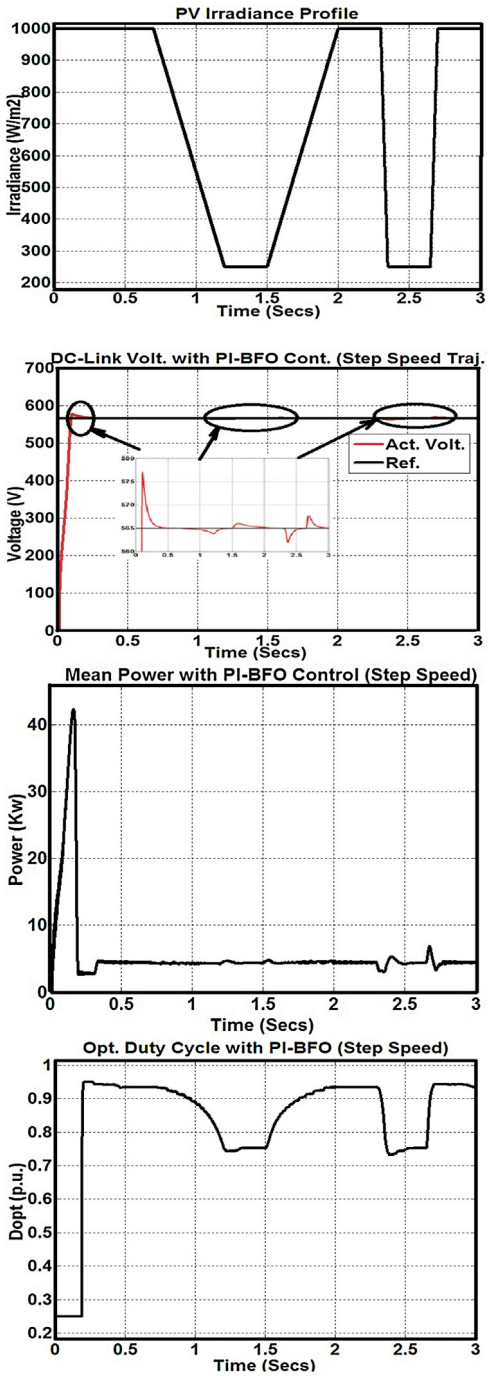

Fig. 16. PV irradiance, dc-link ref. and actual voltage, and PV power with PI-BFO controller.

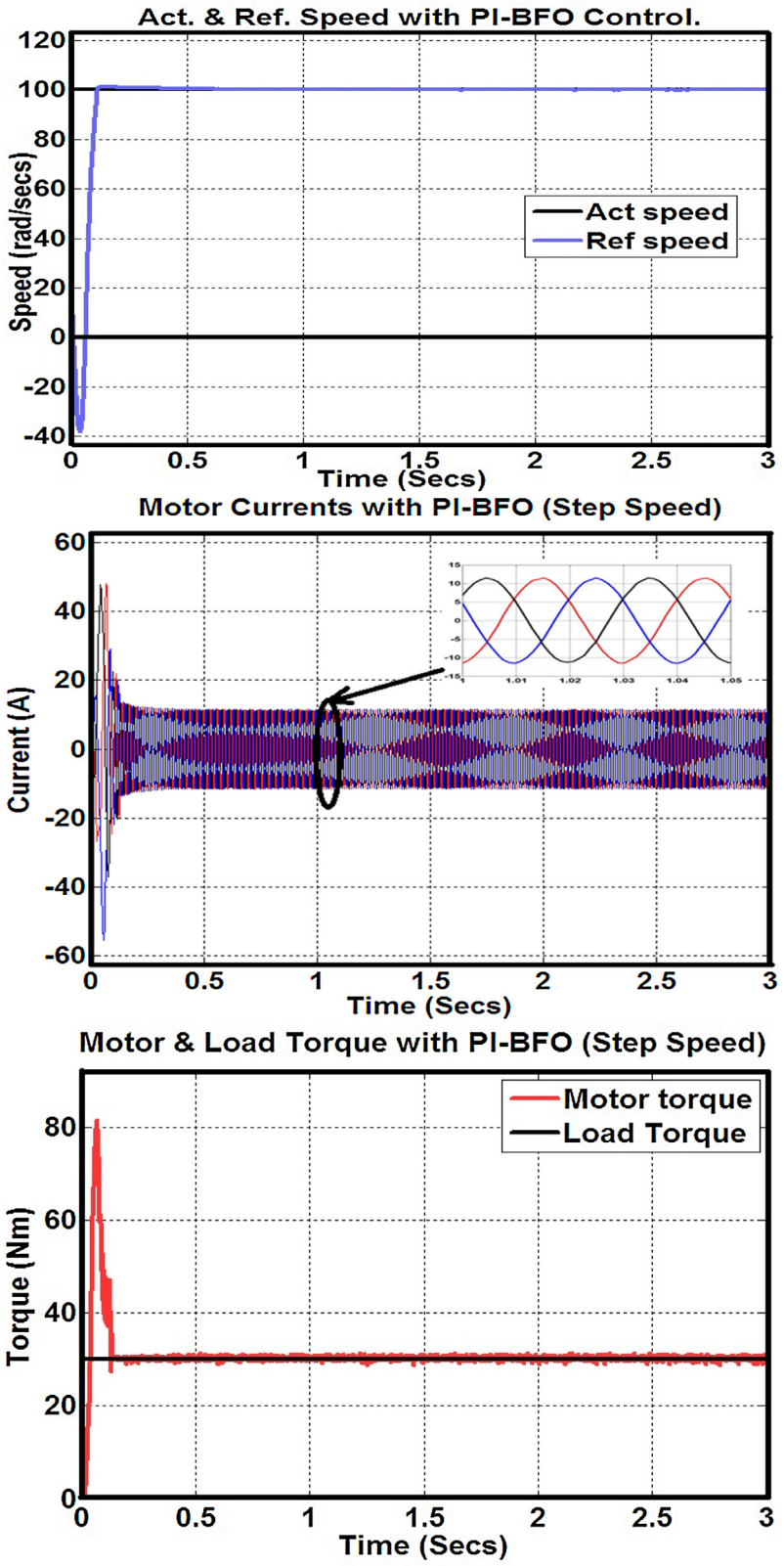

Fig. 17. Motor actual, ref. speed, int., load torque, and phase currents with PI-BFO controller.

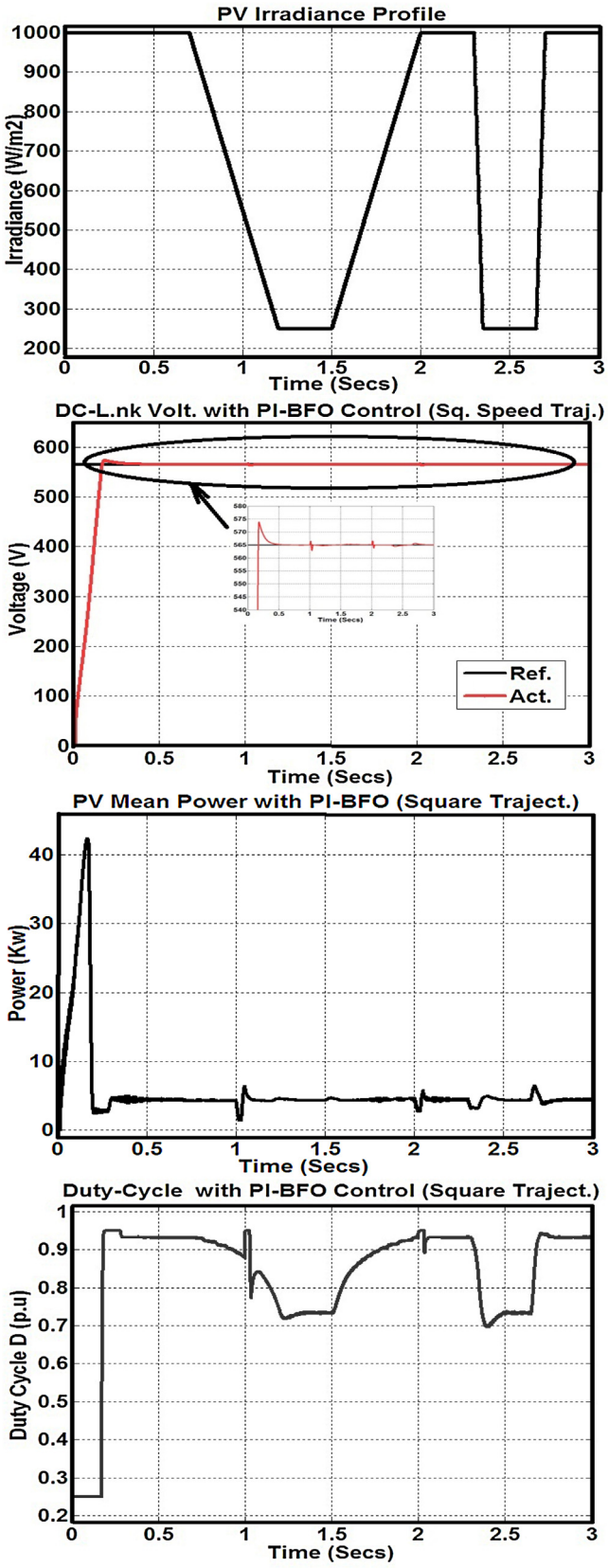

Fig. 18. PV irradiance, power and dc-link actual and reference voltage with square-wave trajectory.

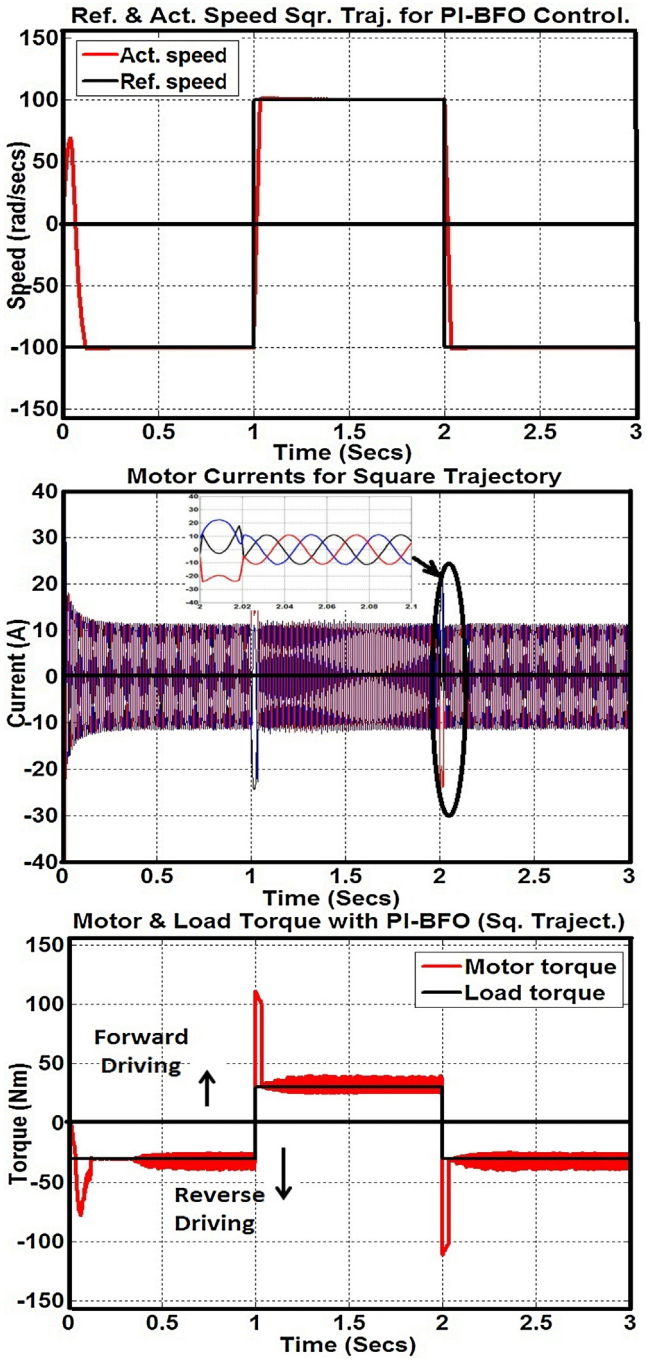

Fig. 19. Motor variables with square wave speed trajectory.

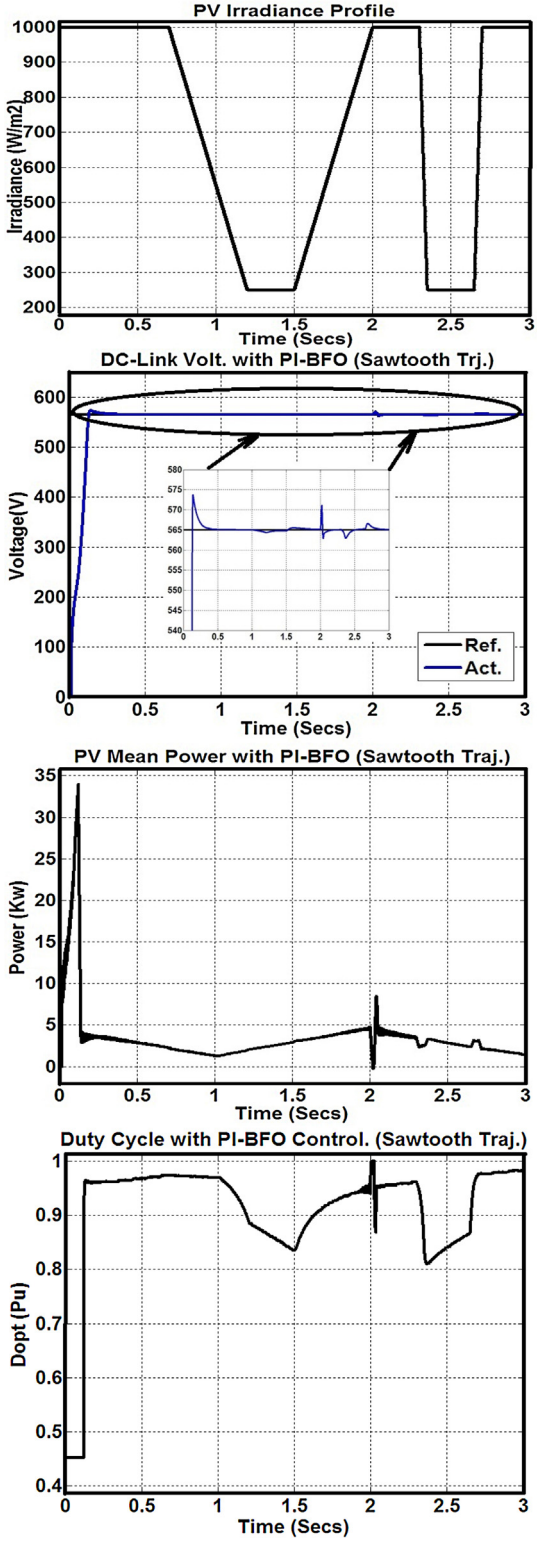

Fig. 20. PV variables and dc-link actual and reference voltages with saw-tooth trajectory.

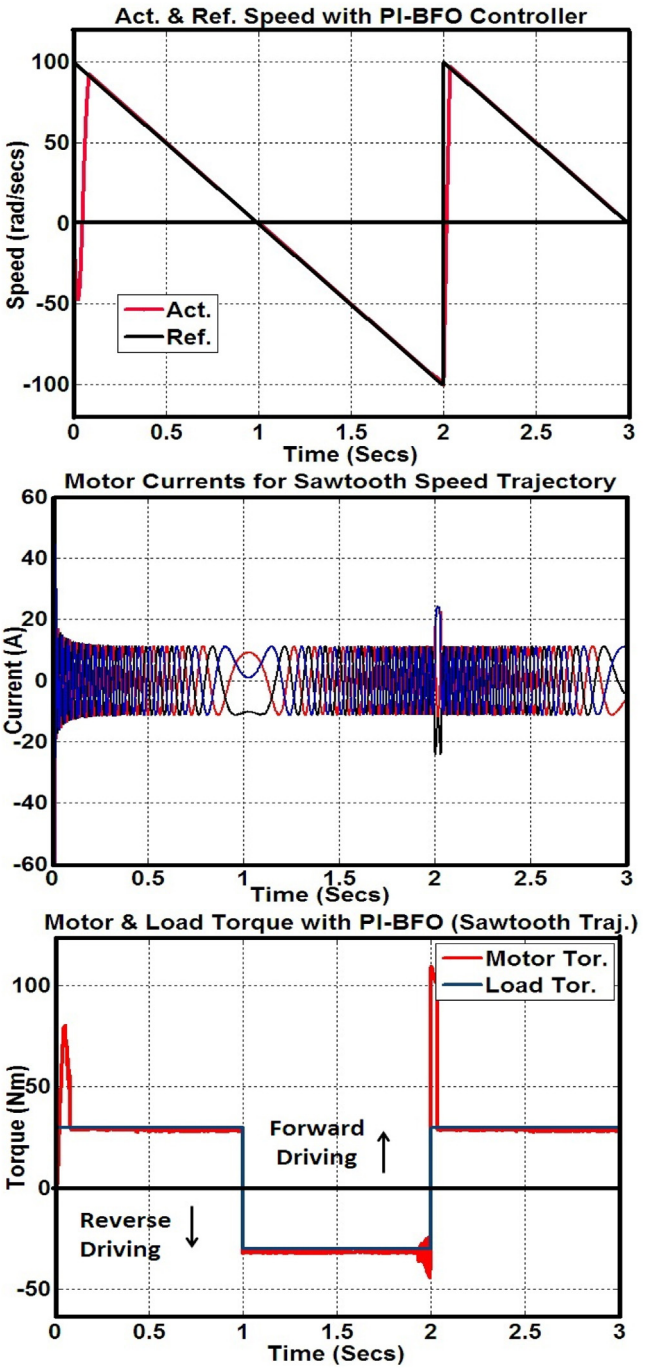

Fig. 21. Motor variables, actual and reference speed with saw-tooth trajectory.

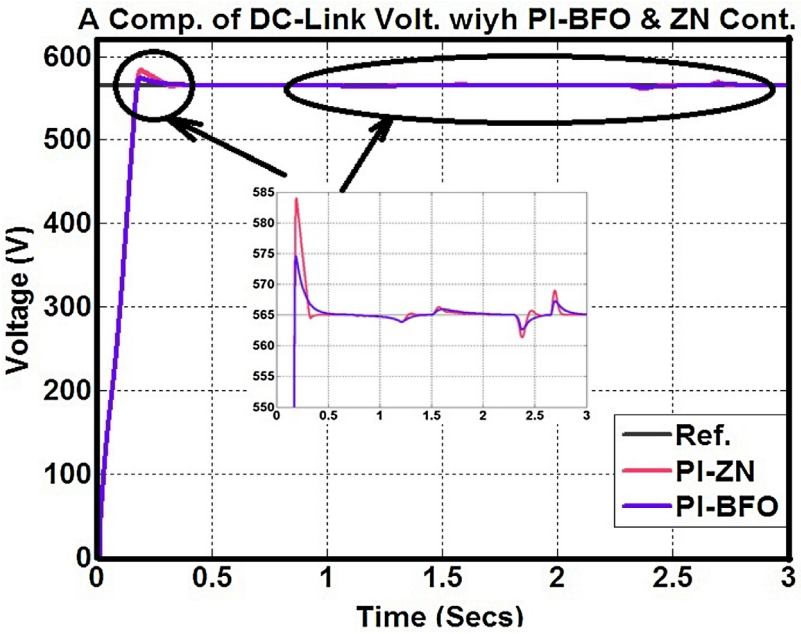

Fig. 22. Actual and reference dc-link voltage curves for PI-BFO and PI-ZN controllers.

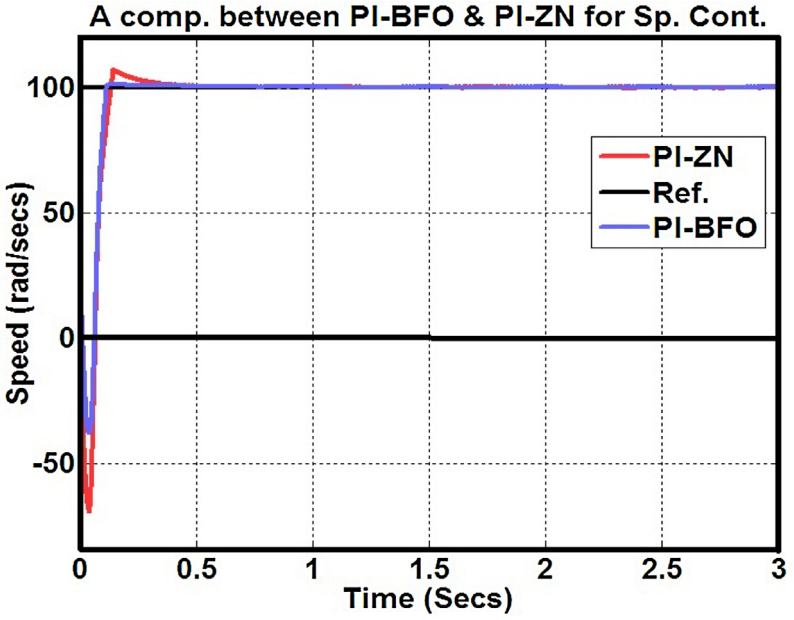

Fig. 23. Actual and reference speed curves for PI-BFO and PI-ZN controllers.

Secondly, Fig. 23 indicates the reference and actual motor speed curves with the proposed PI-BFO and PI-ZN controllers. The maximum overshot in PI-ZN is greater than PI-BFO controllers.

To sum up, the time responses of both the dc-link voltage regulation and motor speed showed tremendous amelioration with the proposed PI-BFO controller rather than classical one.

6. Conclusion and discussion

This paper introduced an optimal-control level-crossing railway-gate tracking drive system fed from PV generator. The proposed system comprises IM-high-performance drive to move the boom barrier up and down, two smart intelligent PI-controllers with self-adaptive self-tuning parameters to optimize the dynamic performance of the whole system. The first one aims to balance between dc-link voltage constancy and MPPT algorithm. The second one contributes toward speed control of the motor to improve its dynamic performance and dependently enhance the performance of the boom barrier against torque ripples and oscillations. This is carried out by both obtaining the optimum duty cycle of the converter and adjusting the modulation index of the inverter. Simulation results show that the performance for both converter/inverter set and motor dynamic response with boom barrier is improved. Moreover, the designed PI-BFO self-tuning self-adaptive controllers are robust against PV-irradiance fluctuation, the load disturbance and oscillation.

Several prescribed speed trajectories are proposed when the PV-irradiance is fluctuated. From the results, the system behaves a superb performance for all speed trajectories compared with classical PI-ZN controllers or when the motor is directly fed from the PV array.

In short, the proposed system is also valid for most of high-performance tracking applications.

Appendix A.

The motor parameters (3-Φ IM)	
Rated power (P_o)	5.4 HP
Rated voltage (V_r (Δ/Y connection)	230/400 V
Rated speed (N_r)	1430 rpm
Rated frequency (f)	50 Hz
Stator and rotor resistances (R_s, R'_r)	1.4, 1.39 Ω
Stator and rotor reactances (X_s, X'_r)	0.005 Ω
Magnetising reactance (X_m)	0.17 Ω
Rotor moment of inertia (J_m)	0.018 kg m^2
Friction coefficient	0.0029 Nms

Bacteria foraging parameters	
No. of bacteria in the population	$S=6$
Swimming length	$N_s=4$
No. of chemotactic steps	$N_C=4$
No. of reproduction steps	$N_{re}=100$
No. of elimination-dispersal events	$N_{ed}=2$
The probability of the eliminated and dispersal bacteria	$P_{ed}=0.25$
No. of bacteria of the best cost function	$S_r=S/2$

References

Abdul-ghaffar, H.I., Essamudin, A.E., Azzam, M., 2013. Design of PID controller for power system stabilization using hybrid particle swarm-bacteria foraging optimization. WSEAS Trans. Power Syst. 8 (1), 12–23.

Abdul-ghaffar, H.I., Essamudin, A.E., Azzam, M., 2014. Design of PID controller for power system stabilization using ant colony optimization technique. In: MEPCON'14, Cairo, 23–25 December.

Acakpovi, A., Hagan, E.B., 2013. Novel photovoltaic module modelling using Matlab/Simulink. Int. J. Comput. Appl. 83 (December (16)), 27–32.

Boldea, I., Nasar, S., 2000. Vector Control of AC Drives. CRC Press Inc., Florida, USA.

El-Saady, G., El-Sayed, A., Essamudin, A.E., Abdul-Ghaffar, H.I., 2015. Harmonic compensation using on-line bacterial foraging optimization based three-phase active power filter. WSEAS Trans. Power Syst. 10, 73–81.

Esram, T., Chapman, P.L., 2007. Comparison of photovoltaic array maximum power point tracking techniques. IEEE Trans. Energy Convers. 22 (2), 439–449.

Essamudin, A.E., 2001. Artificial Neural Network-based Tracking Adaptive Vector Control of Three-phase Induction-motor Servo Drives, Ph.D. Thesis. Cairo (November).

Essamudin, A.E., 2015. A novel approach of bacteria-foraging optimized controller for DC motor and centrifugal pump set fed from photo-voltaic array. J. Next Gener. Inf. Technol. (JNIT) 6 (February (1)), 21–31.

Essamudin, A.E., 2016a. Artificial bee colony-based design of optimal on-line self-tuning PID-controller fed AC drives. Int. J. Eng. Res. (IJER) 3 (12), 807–811.

Essamudin, A.E., 2016b. A novel approach of an adaptive neuro-PI vector controller fed induction-motor servo drives. In: Proceedings of the 2002 IEEE/RSJ International Conference on Intelligent Robots and Systems EPFL, Lausanne, Switzerland, September 30–October 4, pp. 2181–2186.

Essamudin, A.E., Hammad, N., 2003. Fault analysis of current-controlled PWM inverter fed induction motor drives. In: Proceedings of the 7th International Conference on Properties and Applications of Dielectric Materials, Japan, June 1–5, pp. 1065–1070.

Kassem, A.M., 2011. Modelling, analysis and neural MPPT control design of a PV generator powered DC motor-pump system. WSEAS Trans. Syst. 10 (12), 399–412.

Mathwork Corporation, 2012. Matlab/Simulink 2012, User's Guide. USA.

Masoum, M.A.S., Dehbonei, H., Fuchs, E.F., 2002. Theoretical and experimental analyses of photovoltaic systems with voltage and current-based maximum power-point tracking. IEEE Trans. Energy Convers. 17 (4), 514–522.

Oshaba, A.S., Ali, E.S., Abd Elazim, S.M., 2015. Artificial bee colony algorithm based maximum power point tracking in photovoltaic system. WSEAS Trans. Power Syst. 10, 123–134.

Passino, K.M., 2002. Bio-mimicry of bacterial foraging for distributed optimization and control. IEEE Control Syst. Mag., 52–67.

Pu, Y.R., Chen, L.W., Lee, S.H., 2014. Study of moving obstacle detection at railway crossing by machine vision. Inf. Technol. J. 13 (16), 2611–2618.

Rogers, Everett, 2002. Understanding Buck–boost Power Stages in Switch Mode Power Supplies, Texas Instrument Application Report (November).